Lab on a Chip

PAPER

View Article Online
View Journal | View Issue

Cite this: *Lab Chip*, 2023, **23**, 1825

Organ-on-a-chip with integrated semitransparent organic electrodes for barrier function monitoring†

Denise Marrero, [ab] Anton Guimera, [ab] Laure Maes, [cde] Rosa Villa, [ab] Mar Alvarez *[a] and Xavi Illa *[ab]

Organs-on-a-chip (OoC) are cell culture platforms that replicate key functional units of tissues *in vitro*. Barrier integrity and permeability evaluation are of utmost importance when studying barrier-forming tissues. Impedance spectroscopy is a powerful tool and is widely used to monitor barrier permeability and integrity in real-time. However, data comparison across devices is misleading due to the generation of a non-homogenous field across the tissue barrier, making impedance data normalization very challenging. In this work, we address this issue by integrating PEDOT:PSS electrodes for barrier function monitoring with impedance spectroscopy. The semitransparent PEDOT:PSS electrodes cover the entire cell culture membrane providing a homogenous electric field across the entire membrane making the cell culture area equally accountable to the measured impedance. To the best of our knowledge, PEDOT:PSS has never been used solely to monitor the impedance of cellular barriers while enabling optical inspection in the OoC. The performance of the device is demonstrated by lining the device with intestinal cells where we monitored barrier formation under flow conditions, as well as barrier disruption and recovery under exposure to a permeability enhancer. The barrier tightness and integrity, and the intercellular cleft have been evaluated by analyzing the full impedance spectrum. Furthermore, the device is autoclavable paving the way toward more sustainable OoC options.

Received 28th November 2022,
Accepted 15th February 2023

DOI: 10.1039/d2lc01097f

rsc.li/loc

Introduction

Organs-on-a-chip (OoC) are microfluidic cell culture devices intended to replicate key functional units of tissues.[1] These devices can reproduce tissue-level physiology by displaying cells in a multicellular architecture, introducing *in vivo*-like biomechanical cues, and recapitulating tissue interfaces.[2] In addition, they often incorporate functional readouts that record pivotal information about biological processes to characterize and monitor in real-time the cell microenvironment and state of the tissues.[3,4] OoC are commonly used to model tissue barriers due to their important role in regulating human body homeostasis and their implication in many diseases.[5] Research on tissue barriers might lead to a better understanding of tissue physiology and contribute to the identification of new therapeutic agents while significantly reducing animal testing.[6]

Typically, OoC mimicking cellular barriers consist of two perfusable micro-sized chambers separated by a semipermeable membrane lined by cells.[7–9] Examples here include the intestinal epithelium,[10] blood–brain barrier,[11] blood–retinal barrier,[12] and pulmonary air–liquid interface.[13] In all cases, barrier function evaluation is of utmost importance when analyzing cultured tissues in OoC.[14,15] Biological barriers have intrinsic electrical properties that can provide insight into fundamental biological processes such as tissue permeability and integrity.[16] Electrochemical Impedance Spectroscopy (EIS) has been widely used as a technique to study barrier function since it is label-free, non-destructive, and allows real-time measurements.[17] By analyzing the EIS spectrum relevant parameters can be determined: i) transepithelial/endothelial electrical resistance (TEER, alpha) which is an indicator of cellular junction strength, ii) cellular capacitance which is directly proportional to the surface area of the cultured tissue, and iii) medium conductivity changes.[18–21]

[a] *Instituto de Microelectrónica de Barcelona (IMB-CNM, CSIC), Campus UAB, Bellaterra, 08193, Barcelona, Spain. E-mail: mar.alvarez@imb-cnm.csic.es, xavier.illa@imb-cnm.csic.es*
[b] *Centro de Investigación Biomédica en Red en Bioingeniería Biomateriales y Nanomedicina, Madrid, 50018, Spain*
[c] *Department of Internal Medicine and Pediatrics, Ghent University, Gent, Belgium*
[d] *Ghent Gut Inflammation Group, Ghent University, Ghent, Belgium*
[e] *VIB Center for Inflammation Research, Gent, Belgium*

† Electronic supplementary information (ESI) available. See DOI: https://doi.org/10.1039/d2lc01097f

However, most studies report only on TEER values providing limited information obtained by sampling at a single frequency.[22–24] Moreover, TEER data comparison is difficult across studies, as significant discrepancies exist between reported values. These inconsistencies are due to the normalization of the measured impedance by the cell culture area, assuming that the entire cell culture area contributes equally to the measurement. This assumption is inaccurate as the current density distribution across the tissue barrier is non-homogeneous. Thus, the monitored area does not match the total cell culture area. This is a persistent error when measuring TEER with chopstick electrodes, especially for 12 mm Transwell inserts and larger.[25]

In OoC, electrodes are commonly integrated into the device enclosures on either side of the barrier to monitor barrier function. To allow cell inspection under the microscope, electrodes were designed to be much smaller than the cell culture area. This electrode architecture also generates a non-homogeneous field across the cultured tissue, which ultimately resulted in untrustworthy impedance data. In order to generate a current density distribution such that the entire cell culture area contributes equally to the measurement without impairing the optical inspection, thinner layers of metal can be deposited. However, these semitransparent electrodes present high electrode polarization impedance, which can filter out signal content below the electrode cutoff frequency.[18] In this regard, indium tin oxide has been also used because of its well-known transparency, but it is also influenced by a high electrode polarization impedance.[26] Alternatively, interdigitated electrode configurations based on conventional inorganic materials, such as gold and platinum, have been implemented to maximize the electrode area while ensuring minimal electrode coverage for cell inspection.[19,20,27,28] These electrode configurations are also affected by the electrode polarization impedance. To reduce it, platinum black can be electrodeposited enlarging electrode active surface area.[25,29] Moreover, electrode polarization impedance can be eliminated by using tetrapolar configurations.[18,28,30,31] Although it requires greater complexity in evaluating current density homogeneity and it reduces compatibility with benchtop impedance analyzers.

An alternative material that has been widely used to monitor cellular activity in a wide range of device architectures *in vitro* systems is the organic semiconductor polymer poly(3,4-ethylenedioxythiophene) doped with polystyrene sulfonate (PEDOT:PSS).[32,33] For impedance measurements, PEDOT:PSS has been used to improve the recording performance of opaque electrodes[34,35] since it is less affected by electrode polarization impedance compared to inorganic materials. Furthermore, PEDOT:PSS has also been employed to record electrical activity and perform optical imaging simultaneously in microelectrodes array due to its excellent compromise between the polymer electrical properties and transparency.[36] To the best of our knowledge, PEDOT:PSS has never been used solely to monitor the impedance of cellular barriers while enabling optical inspection in OoC.

In this work, we have developed an OoC with integrated semitransparent PEDOT:PSS electrodes to monitor barrier tissue function. Here, we demonstrate how the device overcomes the limitations of current EIS measurements in OoC. Because of PEDOT:PSS low electrode polarization and its semitransparent nature, the electrodes cover the entire cell culture area providing a homogeneous current distribution. Thus, making the entire tissue equally responsible for the measured impedance. Here, the human intestinal colorectal adenocarcinoma cell line (Caco-2) is cultured under flow conditions where the formation, as well as barrier disruption and recovery under permeability enhancer exposure is monitored. By analyzing the full Caco-2 impedance spectrum, we obtained information on the cell junction strength and intercellular cleft morphology (TEER, alpha), and cell surface area (capacitance). Therefore, we expect this device to be used as a tool to perform impedance measurements across virtually any type of barrier-forming tissue in the frequency range from 10 to 10^5 Hz. Additionally, the device is reusable since it is compatible with standard sterilization processes, which reduces its cost and environmental impact.

Materials and methods

Device fabrication with integrated electrodes

Ti/Au (20 nm/200 nm) ring-shaped electrode tracks were patterned on a 1 mm thick cyclo-olefin polymer (COP) sheet (Microfluidic ChipShop, DE) in an e-beam evaporation process using an adhesive vinyl shadow mask. The Ti layer was used to improve the adhesion between gold and the polymeric substrate. The microfluidic features were defined on the COP sheets by computer numerically controlled milling (MDX-40A, Roland DG Corporation, ES). Before patterning the PEDOT:PSS electrodes, the COP sheets were exposed to oxygen plasma for 1 min (Smart Plasma 80 W-Oxygen, Plasma Technology, DE). Then, a solution containing 93.5% PEDOT:PSS, 5% DMSO, and 1.5% Triton X-100 was drop-casted on the center of the Au-ring and cured at 100 °C for 30 min. Male Mini Luer microfluidic connectors (Microfluidic ChipShop, DE) were bonded to the top COP layer using photocurable silicone adhesive (Loctite) by exposing them under UV light (70 mW cm^{-2}) for 2 min. Silicone sheets of 0.5 mm thickness (Silex Ltd., UK) were placed between the COP layers to seal the device. A commercial semipermeable polyester membrane with 0.4 μm pore size (PET, it4ip) was modified to fit the device. The 47 mm diameter membrane was stuck on top of a double-sided adhesive (Adhesive Research, ARCare 8939). The membranes were then defined with a cell culture area of 33.18 mm^2 using a plotter cutter (CAMM-1 Servo GX-24, Roland DG Corporation, ES). For assembly, the COP sheets and the silicone layers were aligned and bolted together using M2 screws. The entire device except for the membrane and all

the components of the microfluidic setup were autoclaved at 110 °C for 30 min followed by overnight drying at 60 °C.

Electrochemical electrode characterization

The electrodes were characterized by electrochemical impedance spectroscopy (EIS). The electrode impedance was recorded using an impedance/gain-phase analyzer (1260, Solartron Analytical) in combination with an impedance interface (1294, Solartron Analytical) by connecting one electrode as the working electrode (WE) and the other electrode as the counter electrode (CE). For individually electrode characterization, single electrode impedance was measured against a commercial Ag/AgCl CE (CH instruments) with much larger surface area. The impedance was measured using a sinusoidal excitation signal with an amplitude of 10 mV over the frequency range of 0.1 Hz to 100 kHz.

Optical electrode characterization

Optical electrode properties were measured using a UV-vis miniature spectrometer (Ocean Optics) and a halogen light source (HL-2000, Ocean Optics) to determine the light absorbance and transmittance of different volumes of drop-casted PEDOT:PSS electrodes in the range between 200 and 1000 nm. The absorbance was plotted with the following formula:

$$A = \log_{10}(I_0/I)$$

where I_0 is the incident light before it reaches the sample and I is the light emerging from the sample. The transmittance in % was calculated with the following formula:

$$\%T = \frac{I}{I_0}\cdot 100$$

EIS measurements on intestinal cells

The impedance of epithelial cellular barriers grown on the microfluidic devices was recorded using a commercially available potentiostat (PalmSens4). The impedance was measured using a sinusoidal excitation signal with an amplitude of 10 mV in the frequency range from 10 Hz to 100 kHz, which corresponds to the frequency window where the electrode behavior is purely resistive. Impedance measurements were carried out using a bipolar configuration by connecting one electrode as the WE and the other electrode as the CE. EIS measurements were carried out in real-time at 37 °C over a period of 7 days.

Impedance data fitting

The impedance of cellular barriers can be represented as an electric circuit composed of three elements: a constant phase element (CPE) in parallel with a resistor (R_{TEER}) and in series with another resistor (R_s).[17] Three well-differentiated regions can be distinguished across the frequency spectrum. At high frequencies ($>10^5$ Hz), the impedance is controlled by the cell culture medium conductivity (R_s), at intermediate frequencies (100–10^5 Hz) impedance is associated with the cell layer capacitance represented by a CPE. At low frequencies (<100 Hz), impedance is determined by the sum of two ion conductive pathways: the paracellular and transcellular resistance which is in turn associated with the transepithelial/endothelial electrical resistance (TEER). The CPE mathematical expression is:

$$Z_{CPE} = \frac{1}{K(j\omega)^{\alpha}}$$

where j is the imaginary unit, ω is the angular frequency, K is the system admittance, and α is an exponent corresponding to 0 or 1 for an ideal resistor or capacitor, respectively. CPE coefficients, R_{TEER}, and R_s values were calculated by fitting the recorded experimental impedance data using the equivalent electric circuit. The cellular layer capacitance (C_{cl}) was estimated using the following equation:

$$C_{Cl} = \frac{(K\cdot R_{TEER})^{1/\alpha}}{R_{TEER}}$$

Impedance data recorded from epithelial cellular barriers grown on the microfluidic device was fitted to the equivalent electric circuit using the least-square method in Python. Data was assessed by the goodness-of-fit (χ^2) statistical model, and all data fitted well with a $\chi^2 < 0.01$.

Epithelial cell culture

The human intestinal colorectal adenocarcinoma cell line (Caco-2, ECACC) was maintained in a humified atmosphere with 5% CO_2 at 37 °C in the recommended medium MEM alpha with Glutamax-I medium (Sigma-Aldrich) supplemented with 10% fetal bovine serum (Sigma-Aldrich). At 70–80% of confluency, cells were washed with PBS, detached with 0.05% trypsin/ethylenediaminetetraacetic acid (Life Technologies), pelleted at 1400 rpm for 5 min. Media was replaced every 2–3 days.

Microfluidic cell culture

The PET membrane was coated with type I collagen (Inycom) at a concentration of 100 μg ml^{-1} for 1 h to enhance cell adhesion. 50 000 Caco-2 cells were seeded on the upper surface of the PET membrane and cultured in medium containing 1% of antibiotic–antimycotic (Sigma). After 4 h, the devices were assembled and connected to the perfusion system. A peristaltic pump (Reglo ICC, ISMATEC, Cole-Parmer GmbH) was attached and 0.81″ inner diameter silicone tubing (Freudenberg Medical) were used to make all the microfluidic connections. The lower channel was perfused continuously at 20 μl min^{-1}. On the upper channel, 500 μl of medium was perfused every 3 hours at 20 μl min^{-1}.

To induce temporary epithelial barrier loss, 4 mM EDTA was perfused on the upper channel using a Luer injection port (AI-10820, Inycom) during 30 min. Images of Caco-2 cells cultured inside the device were taken with an inverted microscope (ECLIPSE TS2, Nikon).

Immunohistochemistry

Cells cultured on the PET membrane were washed twice with PBS and subsequently fixed for 10 min in 4% paraformaldehyde. After fixation, cells were washed with PBS and the membrane was cut and placed in a 24-well plate. Next, cells were permeabilized for 5 min with 1% Triton X-100 (Sigma-Aldrich) in PBS and after two washing steps with PBS, blocked for 20 min with 2% bovine serum albumin in PBS. The membranes were incubated with the primary and the secondary antibodies in blocking buffer for 2 h and 1 h, respectively with two washing steps in between. After another two washing steps, nuclei were stained with DAPI (300 nM; Sigma-Aldrich, D9542) for 15 min. The following primary antibodies were used: rabbit ZO-1 (1 μg ml^{-1}, Sigma-Aldrich, HPA001636) and goat villin-2 (2.5 μg ml^{-1}, Bio-Rad, AHP1394). The following secondary antibodies were used: chicken anti-rabbit-488 (1 μg ml^{-1}, Sigma-Aldrich, SAB4600030) and chicken anti-goat-647 (1 μg ml^{-1}, ThermoFisher, A-21469). All steps were performed at room temperature. Imaging was performed after two additional washing steps with an Olympus FluoView confocal microscope. Images were processed in Fiji (ImageJ).

Results and discussion

Device design

The device was designed to monitor and quantify cellular barrier function using impedance-based techniques in a microfluidic OoC (Fig. 1a). Cyclo-olefin polymer (COP) was used as a substrate for its biocompatibility, transparency, chemically resistance to polar solvents, high glass transition temperature, compatibility with rapid prototyping techniques, and metal deposition procedures.[37] The device contains a 6.5 mm diameter well yielding an area of 33.18 mm^2 (comparable with conventionally Transwell® cell culture inserts). The well is embedded on an upper channel (25 mm long × 2.6 mm wide × 1 mm high) and sitting on the lower channel (30.3 mm long × 2.6 mm wide × 1 mm) separated by a semipermeable PET membrane (Fig. 1b). The membrane is sandwiched between two COP substrates with integrated PEDOT:PSS electrodes on the device enclosures. The integrated electrodes were fabricated combining standard metal gold patterning and PEDOT:PSS drop-casting techniques, as described in the previous section. The electrodes were designed to comprise two parallel electrodes (bipolar configuration), one located above the well and the other below the cell culture membrane. The bipolar configuration demands a very simple measuring setup resulting in high compatibility with benchtop impedance analyzers. The two electrodes have a circular design comprising the same area of the cell culture membrane to ensure a uniform current density across the cellular barrier. Hence, the entire cellular membrane contributes equally to the measured impedance. Moreover, the device can be sterilized by autoclaving except for the cell culture membrane and is resistant to ethanol exposure (Fig. S1†).

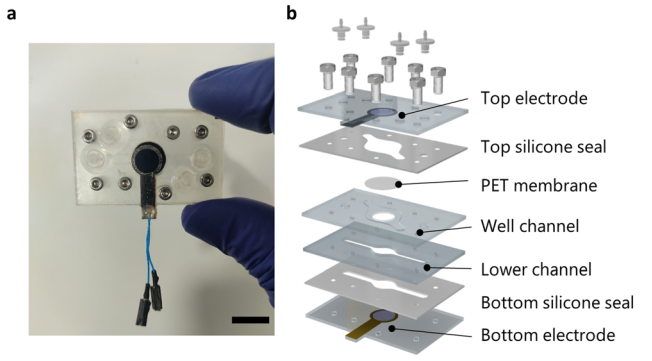

Fig. 1 Organ-on-a-chip design with integrated PEDOT:PSS electrodes (scale bar = 1 cm). a) Photograph of the microfluidic device with incorporated PEDOT:PSS electrodes. b) Exploded view of the microfluidic cell culture device.

Optical electrode characterization

Optical access in cell culture is very important to monitor the cells throughout time. The drop-casted PEDOT:PSS electrodes display high optical transmittance for cellular optical microscopy. The degree of electrode transmittance and storage capacity was investigated in relation to PEDOT:PSS drop-casting volume. According to the absorbance spectrum of PEDOT:PSS electrodes is dependent on the incident wavelength and presents a peak of absorbance at 680 nm (Fig. S2†). Transmittance decreases along with higher drop-casting volume (Fig. 2a). Moreover, the area under the CV curve increases along with the drop-casting volume, indicating a larger electrode active surface area (Fig. 2b).

Electrochemical electrode characterization

In order to validate electrode performance in monitoring tissue barrier function in OoC, several impedance-based tests were conducted. The impedance spectra of PEDOT:PSS electrodes were recorded using 10 mM PBS from 0.1 Hz to 10^5 Hz. The recorded spectra or Bode plot describes the electrode polarization impedance, representing the impedance at the electrode–electrolyte interface. The Bode plot display two distinct regions (Fig. 3a). At high frequencies, the impedance depends directly on the ion solution conductivity. At low frequencies, signal content is dominated by the double-layer capacitance at the electrode–electrolyte interface, which results in a non-linear attenuation of the signal. The cutoff frequency marks the transition from low to high impedance and is defined as the frequency corresponding to a phase angle of −45°. The cutoff frequency is 1.5 Hz for PEDOT:PSS electrodes with a surface area of

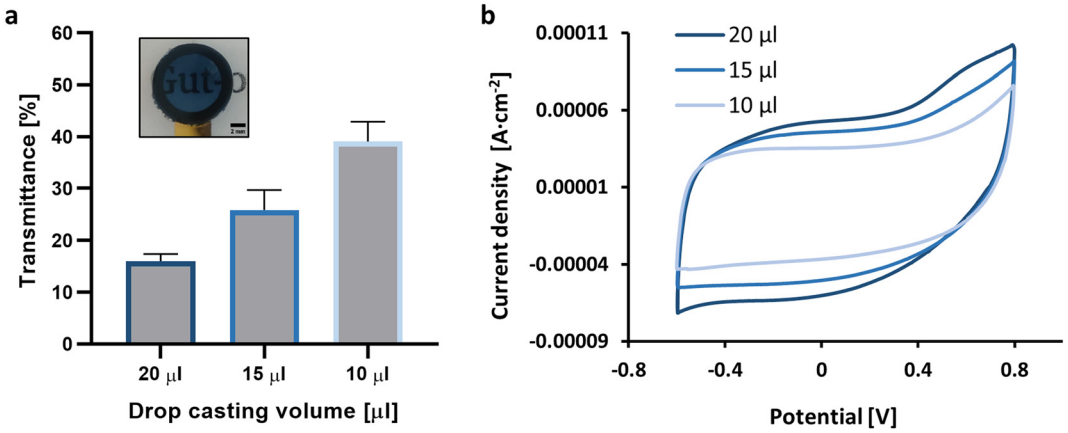

Fig. 2 Optical electrode characterization a) drop-casted PEDOT:PSS in relation to its transmittance at its maximum absorbance peak (n = 3). (Inset) Photograph of the drop-casted PEDOT:PSS electrode showing its semitransparency with a drop-casting volume of 15 µl. b) Cyclic voltammetry of different drop casted volumes.

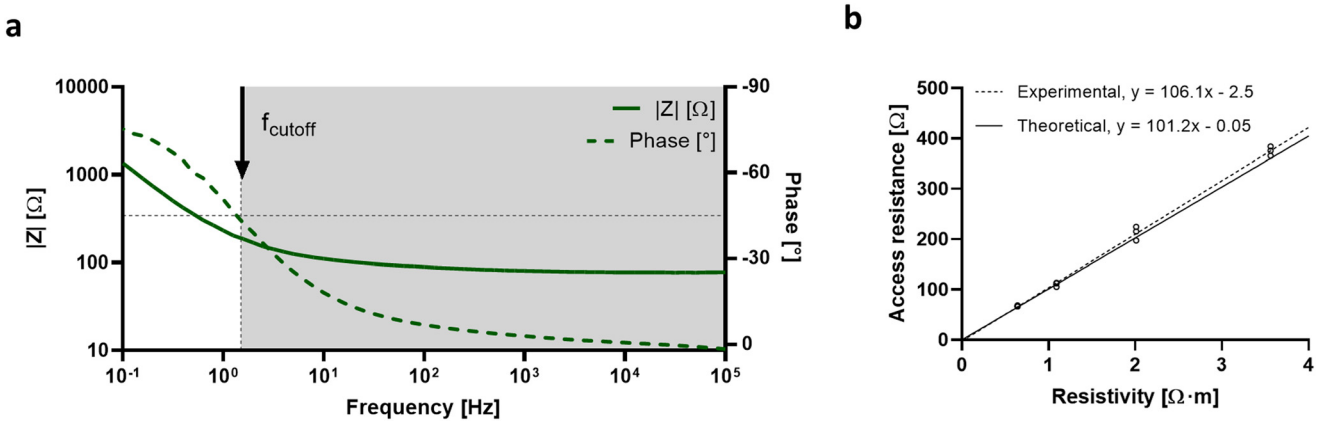

Fig. 3 Electrochemical characterization of PEDOT:PSS electrodes. a) Representative impedance spectra of drop casted PEDOT:PSS electrodes with gold tracks under 10 mM PBS solution (n = 10). The colored area indicates the frequency range at which the electrodes display a resistive response being above the cutoff frequency (1.5 Hz). b) The experimental cell constant (K_e) of the build-in electrodes is represented by the dashed line. Impedance was measured with the device assembled at different PBS resistivities of 3.56, 2.01, 1.09, and 0.64 Ω m which corresponds to a PBS molarity of 1.25, 2.5, 5, and 10 mM, respectively (n = 3). The theoretical cell constant (K_e) of the build-in electrodes is represented by the solid line.

33.18 mm^2. Furthermore, the impedance spectra were recorded using different PBS molarities to determine if the electrodes were responsive to changes in electrolyte resistivity (Fig. S3†). By plotting the measured resistance of each PBS molarity at high frequencies against the corresponding electrolyte resistivity, the experimental device cell constant (K_e) was obtained according to the following expression:

$$K_e = \frac{R}{\rho} \left[m^{-1}\right]$$

where R is the access resistance in Ω and ρ the electrolyte resistivity in Ω m. The K_e is linear and proportional to electrolyte resistivity. Also, the K_e was compared to the theoretical cell constant (K_t) and was calculated according to the following expression:

$$K_t = \frac{A}{d} \left[m^{-1}\right]$$

where d is the distance between the two electrodes in m and A is the surface area of the electrode in m^2. The experimental cell constant was calculated to be 106.1 m^{-1}, which is in agreement with the theoretical value (Fig. 3b). The linearity of the cell constant and the fact that the theoretical and the experimental values match demonstrates that the current distribution generated by the PEDOT:PSS electrodes is homogeneous across the tissue culture area and the entire area is equally accountable for impedance measurements. As a result of the low electrode polarization impedance and homogeneous current distribution, PEDOT:PSS electrodes are suitable for EIS measurements on OoC.

Intestinal barrier development and integrity assessment

To evaluate electrode performance, the human intestinal colorectal adenocarcinoma cell line (Caco-2) was cultured on

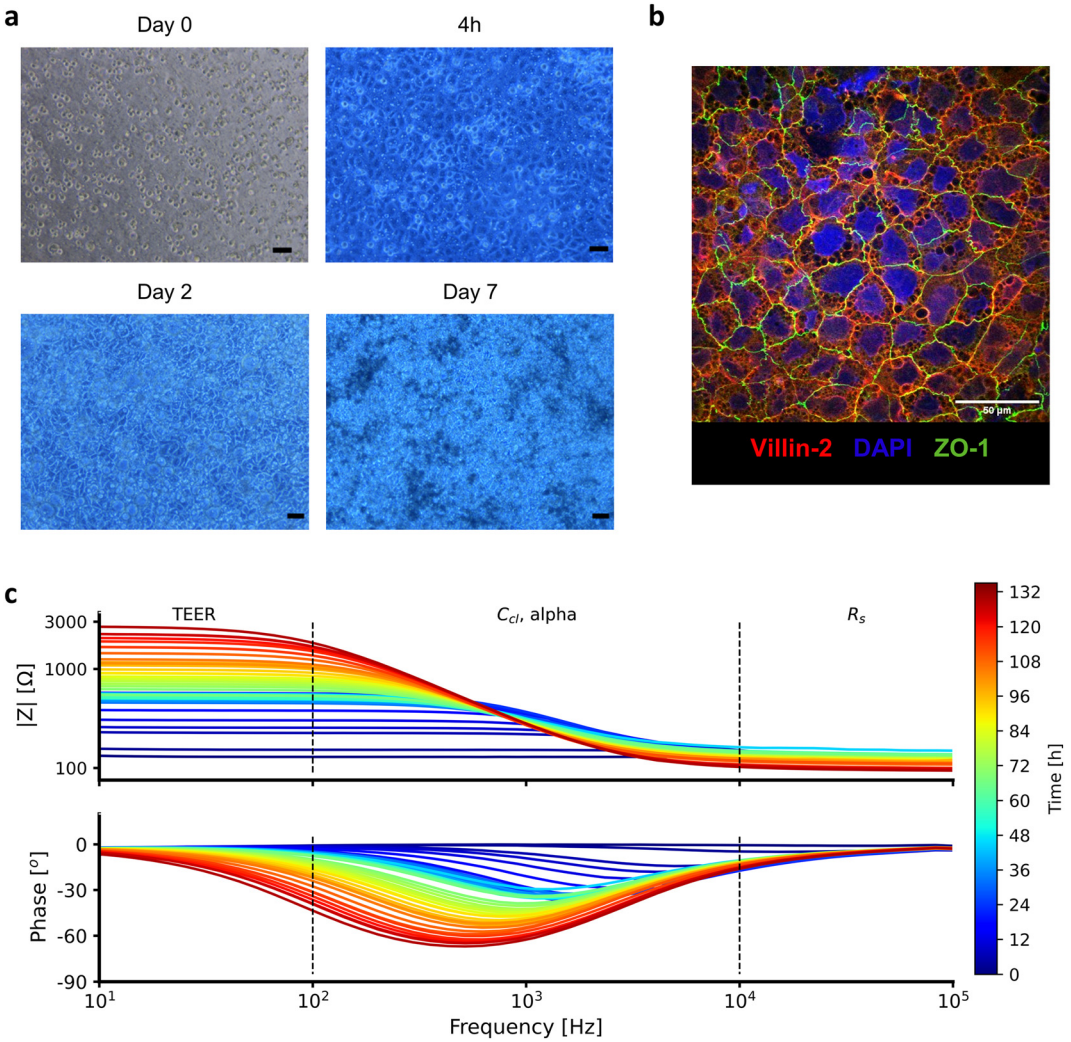

Fig. 4 a) Microscopic images of the development of a Caco-2 monolayer at different timepoint (scale bar = 50 μm). b) Maximum intensity projection of confocal image of an immunofluorescent labeled monolayer for DAPI, ZO-1, and villin-2 at day 7 of microfluidic culture. c) Experimental impedance data recorded during 6 days of Caco-2 microfluidic cell culture inside the developed device with integrated PEDOT:PSS electrodes. The cellular barrier impedance was measured over the frequency range of 10 to 10^5 Hz and the impedance spectra is plotted every 3 hours. The impedance at low frequencies ($<10^2$ Hz) corresponds to the transepithelial/endothelial electrical resistance (TEER) and the overall device resistance, the impedance negative slope at intermediate frequencies (10^2–10^4 Hz) is related to the cellular capacitance, and at high frequencies ($>10^4$) the impedance corresponds to the device resistance.

the device under flow conditions. Fig. 4a shows microscopic images of the formation and maturation of the monolayer at different time points. On day 0, cells were seeded on a collagen-coated semipermeable PET membrane. After 4 h, cells were attached to the PET membrane and started expanding to form a confluent monolayer. From day 2 to day 7, the first signs of intestinal maturation were visible including the production of mucus, the formation of vacuoles, and an increase in cell height, which is in agreement with previous studies.[38,39] Immunofluorescence microscopy of the tight junction protein zonula occludens-1 (ZO-1), and a protein supporting microfilaments of the microvilli, villin-2, confirmed that Caco-2 cells form tight junctions and microvilli structures. This indicates that Caco-2 cells proliferate and differentiate into a polarized tight barrier (Fig. 4b). Next, the impedance of the Caco-2 cells was monitored for one week in real-time with a commercially available analyzer (PalmSens4). Fig. 4c shows the impedance spectra of Caco-2 cells during the initial stages of cellular barrier formation and development. The impedance spectra display three distinct regions. At high frequencies ($>10^4$ Hz), the contribution is manly resistive due to medium, membrane, and electrode resistance, R_s. Fluctuation of this value can be attributed to changes in medium conductivity or temperature variations. At intermediate frequencies (10^2–10^4 Hz), the change in impedance is associated with the cellular membrane capacitance, C_{cl}. This parameter is related to the cellular surface area and enables the identification of complex structures such as microvilli.[18,40] Below 10^2 Hz, the impedance is an indicator of ion conductance of the

paracellular pathway modulated by tight junction protein complexes and is related to cellular barrier integrity, TEER.[14] Hence, when Caco-2 cells are seeded on top of the PET membrane, the impedance resembles a flat line. As Caco-2 cells start to grow and mature, they establish physical connections with neighboring cells and strengthen cell-to-cell bonds. Then, the impedance spectrum transitions to a negative slope along with an increase in resistance at low frequencies as a result of confluent monolayer formation and cellular barrier tightening.

Electrical properties of intestinal barriers

By fitting the equivalent electric circuit composed of a CPE (C_{cl}, alpha) in parallel with a resistor (R_{TEER}) and in series with another resistor (R_s) to the impedance data, the electrical properties of Caco-2 cells were extracted (Fig. 5a). The recorded impedance data of Caco-2 cells cultured in the device fitted with high accuracy the proposed equivalent electric circuit (Fig. S4†). As demonstrated by the cell constant test (Fig. 3b), the entire cellular barrier is equally accountable for impedance measurements. Therefore, we present with confidence TEER and capacitance values normalized by the cellular barrier surface. For the first 3 days of culture, TEER values increased steadily from 20 Ω cm^2 to 1000 Ω cm^2, indicative of barrier development and tightening. After day 3, TEER values stabilized to an average of 1000 Ω cm^2 (Fig. 5c). Capacitance values followed the same trend with a constant increase from 0.5 μF cm^{-2} on day 0 up to 2 μF cm^{-2} on day 3, followed by a plateau until day 7 (Fig. 5d). The specific capacitance is well reported to be relatively constant at 1 μF cm^{-2} for flat cellular membranes.[41] Since the capacitance is proportional to the surface area, the capacitance of mature Caco-2 monolayers indicates that the total area has increased by 2-fold. In our cellular model, the increase can be attributed to the formation of microvilli at the apical domain of the cell layer as can be confirmed by the presence of villin-2 (Fig. 4b).[42,43] Moreover, the dimensionless alpha parameter of the CPE models the frequency dependency of the associated capacitance. This parameter can be used to describe the intercellular cleft of adjacent cells as illustrated in Fig. 5b.[44] A value close to 1 indicates that the basolateral side is in full contact with neighboring cells and the substrate.[21] If alpha is less than 1, it denotes that the basolateral side is no longer in contact with its neighboring cells, presenting grooves that prevent the passage of high-frequency current. In our model, alpha increased steadily from 0.85 on day 0 to stabilizing at 0.97 on day 2. This indicates that at the beginning of Caco-2 development, cells are not as tightly packed, which is

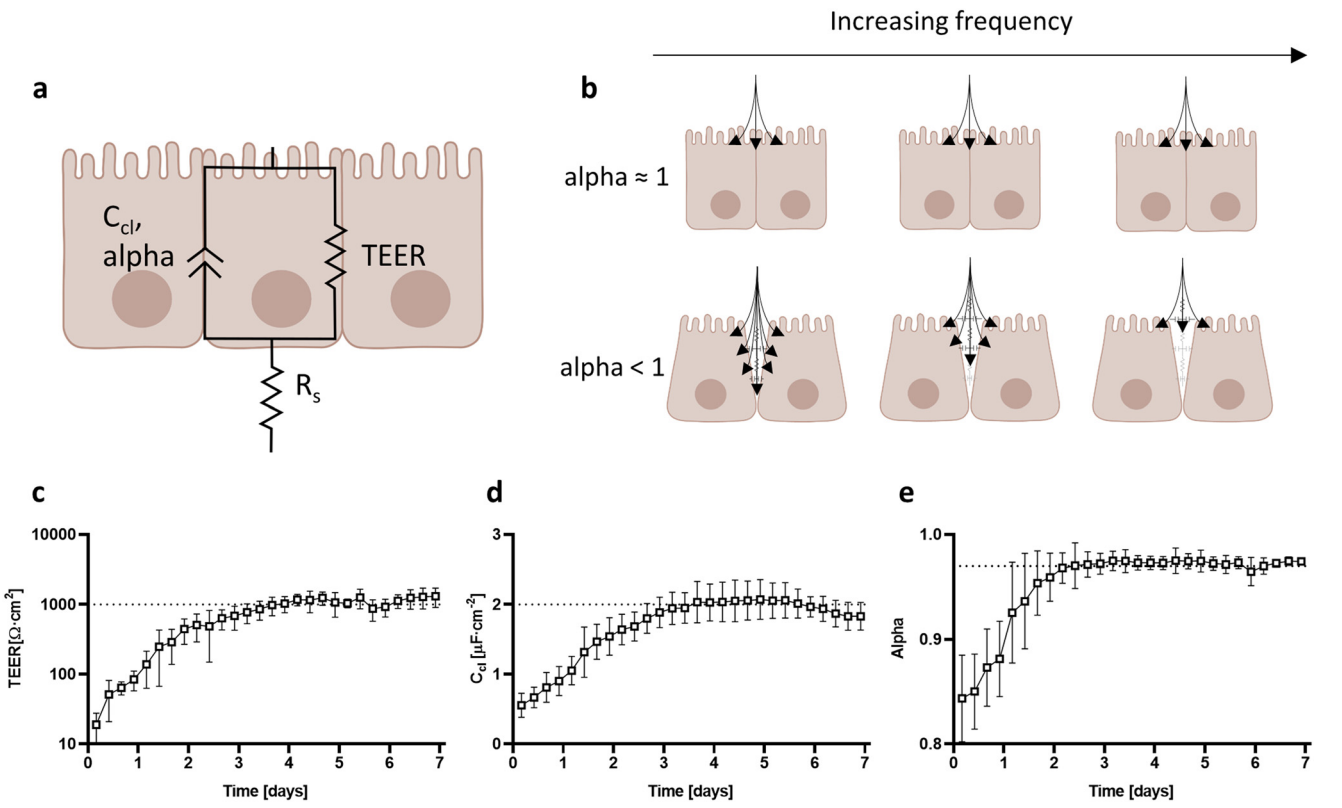

Fig. 5 Electrical properties of Caco-2 cells. a) Equivalent electric circuit of cellular barriers. b) A representation of the intercellular cleft in relation to alpha. Increasing frequency does not affect the current penetration of monolayers with alpha close to 1. Conversely, the current penetration of monolayers with lower alpha decreases as frequency increases. Extracted bioelectrical properties of Caco-2 cells overtime by fitting the impedance spectra to an equivalent electric circuit (n = 4). c) TEER [Ω cm^2], d) Cellular capacitance [μF cm^{-2}], and e) factor alpha (dimensionless).

consistent with lower TEER values. After day 3, matured Caco-2 cells grow with a very narrow intercellular cleft (Fig. 5e).

Response of Caco-2 cells to EDTA chelating agent

To study the permeability of the Caco-2 monolayer in the OoC device and to further evaluate the performance of the fabricated electrodes, Caco-2 cells were exposed to 4 mM EDTA for 30 min. Impedance was monitored in real-time during impedance drop and recovery of Caco-2 monolayers. In cell culture, EDTA works as a chelating agent by capturing metal ions such as calcium and magnesium from the media, thereby weakening cell adhesion, and increasing cellular permeability. Different molarities of EDTA were tested on Caco-2 monolayers grown for 7 days in static conditions to evaluate its effect on cell layer integrity (Fig. S5†). For the on-chip experiments, a concentration of 4 mM was used to ensure cell-to-cell bond conservation and cell-to-membrane adhesion, although some morphological changes were observed. As Tomita *et al.* reported, these changes are attributed to microfilament contraction upon EDTA exposure.[45] The electrodes recorded a TEER drop of 50% in response to EDTA exposure due to an increase in paracellular permeability (Fig. 6a). After perfusing EDTA-free medium, TEER values returned to their previous levels after approximately 2 h. This is in accordance with previous studies in static cultures and on OoC using absorption enhancers.[19,46] In contrast with TEER decline, capacitance rapidly increased by 30% immediately after EDTA injection. An increase in capacitance results from the rearrangement of actin microfilaments, which affects cell morphology and also could cause a few cells to detach resulting in irregular or rough monolayers. During EDTA exposure, capacitance values restore their initial values. After EDTA exposure, capacitance drop can be attributed to some loss of tissue maturation. After one hour of free-EDTA medium exposure, the capacitance returned to its initial values (Fig. 6b). The alpha parameter undergoes a fast drop during the EDTA exposure, up to a 15% decrease (Fig. 6c). Because alpha is related to the intercellular cleft, its drop is an indication of a decrease in the cell-to-cell and cell-to-membrane contact area. Finally, after finishing the EDTA exposure, alpha values quickly recovered to pre-EDTA levels. This is consistent with the requirement to regain cell-to-cell contact, followed by barrier tightening. Alpha is a complementary parameter for tracking and monitoring changes in cellular barrier permeability. Moreover, it is dimensionless, making it suitable for better comparison across different OoC.

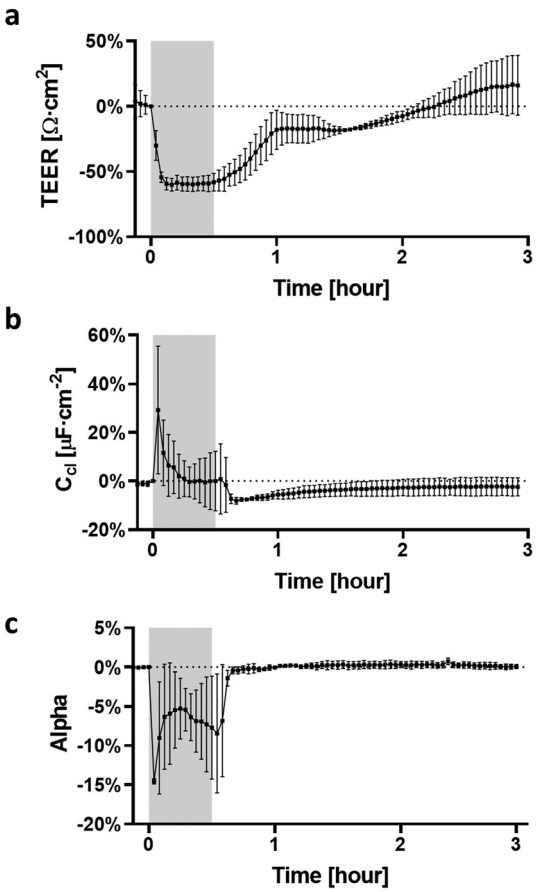

Fig. 6 Effect of 4 mM EDTA on a) TEER, b) capacitance, and c) alpha values of Caco-2 cells. The gray area indicates EDTA time exposure. Caco-2 cells were grown for 7 days on the device after being exposed at the apical side to 4 mM EDTA. 1 ml EDTA was injected into the microfluidic with an injection port. After 30 min of EDTA exposure, 500 μL of DMEM was perfused at 20 μL min^{-1} (n = 3).

Conclusion

In this work, we have engineered an OoC device with integrated semitransparent PEDOT:PSS electrodes that perform impedance measurements over a frequency range relevant to cell culture while allowing optical inspection. We demonstrate that PEDOT:PSS is an ideal material for electrode integration into OoC to perform EIS measurements given its excellent compromise between low electrode polarization impedance and high electrode transmittance. Moreover, we show that PEDOT:PSS can be easily integrated into OoC by using rapid prototyping techniques such as milling and drop-casting.

Electrode integration into OoC is more informative and robust than relying on single-frequency measurements with chopsticks-like electrodes. Exploiting the full frequency spectrum for barrier function monitoring provides quantifiable information about cellular behavior and barrier tissue properties. In this work, the device is used to monitor in real-time the development and maturation of intestinal cells, being able to track changes in impedance upon exposure to a permeability enhancer. The device and electrode design, apart from preserving the optical visualization of the cell culture, guarantee a homogeneous current distribution across the entire cultured tissue making the entire cell culture area equally accountable for impedance measurements. Therefore, we can present with confidence

EIS data normalized by the surface area. This study opens the way toward a better comparison among impedance data standardize impedance measurements on an OoC.

Author contributions

Denise Marrero: conceptualization, investigation, writing – original draft; Anton Guimera: formal analysis, software, writing – review & editing; Laure Maes: investigation; Rosa Villa: funding acquisition; Mar Alvarez: funding acquisition, supervision, writing – review & editing; Xavi Illa: supervision, writing – review & editing.

Conflicts of interest

The authors declare that there are no conflicts of interest.

Acknowledgements

The authors acknowledge the support from the Ministerio de Ciéncia Innovación y Universidades (MICIU/FEDER, EU), in Spain, through GUMICHIP project (RTI2018-096786-B-I00). Denise Marrero acknowledges that this work has been done in the framework of the Ph.D. program in Electrical and Telecommunication Engineering at the Universitat Autònoma de Barcelona and was supported by the FPI Ph.D. fellowship (PRE2019-089214). This work has made use of the Spanish ICTS Network MICRONANOFABS partially supported by MICINN and the ICTS 'NANBIOSIS', more specifically by the Micro-NanoTechnology Unit of the CIBER in Bioengineering, Biomaterials and Nanomedicine (CIBER-BBN) at the IMB-CNM. Microfluidic cell culture was performed at Servei de Cultius Cel·lulars, Producció d'Anticossos i Citometria (SCAC) belonging to Universitat Autònoma de Barcelona (UAB).

References

1 D. Huh, B. D. Matthews, A. Mammoto, M. Montoya-Zavala, H. Y. Hsin and D. E. Ingber, *Science*, 2010, **328**, 1662–1668.
2 S. N. Bhatia and D. E. Ingber, *Nat. Biotechnol.*, 2014, **32**, 760–772.
3 Y. Zhu, K. Mandal, A. L. Hernandez, S. Kawakita, W. Huang, P. Bandaru, S. Ahadian, H.-J. Kim, V. Jucaud, M. R. Dokmeci and A. Khademhosseini, *Curr. Opin. Biomed. Eng.*, 2021, **19**, 100309.
4 D. Marrero, F. Pujol-Vila, D. Vera, G. Gabriel, X. Illa, A. Elizalde-Torrent, M. Alvarez and R. Villa, *Biosens. Bioelectron.*, 2021, **181**, 113156.
5 C. M. Sakolish, M. B. Esch, J. J. Hickman, M. L. Shuler and G. J. Mahler, *EBioMedicine*, 2016, **5**, 30–39.
6 S. Jalili-Firoozinezhad, C. C. Miranda and J. M. S. Cabral, *Trends Biotechnol.*, 2021, **39**, 838–852.
7 B. Jing, Z. A. Wang, C. Zhang, Q. Deng, J. Wei, Y. Luo, X. Zhang, J. Li and Y. Du, *Front. Bioeng. Biotechnol.*, 2020, **8**, 272.
8 W. Shin, A. Wu, M. W. Massidda, C. Foster, N. Thomas, D.-W. Lee, H. Koh, Y. Ju, J. Kim and H. J. Kim, *Front. Bioeng. Biotechnol.*, 2019, **7**, 13.
9 S. Jalili-Firoozinezhad, F. S. Gazzaniga, E. L. Calamari, D. M. Camacho, C. W. Fadel, A. Bein, B. Swenor, B. Nestor, M. J. Cronce, A. Tovaglieri, O. Levy, K. E. Gregory, D. T. Breault, J. M. S. Cabral, D. L. Kasper, R. Novak and D. E. Ingber, *Nat. Biomed. Eng.*, 2019, **3**, 520–531.
10 H. J. Kim, H. Li, J. J. Collins and D. E. Ingber, *Proc. Natl. Acad. Sci. U. S. A.*, 2016, **113**, E7–E15.
11 T.-E. Park, N. Mustafaoglu, A. Herland, R. Hasselkus, R. Mannix, E. A. FitzGerald, R. Prantil-Baun, A. Watters, O. Henry, M. Benz, H. Sanchez, H. J. McCrea, L. C. Goumnerova, H. W. Song, S. P. Palecek, E. Shusta and D. E. Ingber, *Nat. Commun.*, 2019, **10**, 2621.
12 J. Paek, S. E. Park, Q. Lu, K.-T. Park, M. Cho, J. M. Oh, K. W. Kwon, Y. Yi, J. W. Song, H. I. Edelstein, J. Ishibashi, W. Yang, J. W. Myerson, R. Y. Kiseleva, P. Aprelev, E. D. Hood, D. Stambolian, P. Seale, V. R. Muzykantov and D. Huh, *ACS Nano*, 2019, **13**, 7627–7643.
13 V. V. Thacker, N. Dhar, K. Sharma, R. Barrile, K. Karalis and J. D. McKinney, *eLife*, 2020, **9**, e59961.
14 B. Srinivasan, A. R. Kolli, M. B. Esch, H. E. Abaci, M. L. Shuler and J. J. Hickman, *J. Lab. Autom.*, 2015, **20**, 107–126.
15 K. Benson, S. Cramer and H.-J. Galla, *Fluids Barriers CNS*, 2013, **10**, 5.
16 S. Grimnes, *Bioimpedance and bioelectricity basics*, Elsevier, Boston, MA, 2014.
17 B.-Y. Chang and S.-M. Park, *Annu. Rev. Anal. Chem.*, 2010, **3**, 207–229.
18 M. W. van der Helm, O. Y. F. Henry, A. Bein, T. Hamkins-Indik, M. J. Cronce, W. D. Leineweber, M. Odijk, A. D. van der Meer, J. C. T. Eijkel, D. E. Ingber, A. van den Berg and L. I. Segerink, *Lab Chip*, 2019, **19**, 452–463.
19 O. Y. F. Henry, R. Villenave, M. J. Cronce, W. D. Leineweber, M. A. Benz and D. E. Ingber, *Lab Chip*, 2017, **17**, 2264–2271.
20 J. Yeste, L. Martínez-Gimeno, X. Illa, P. Laborda, A. Guimerà, J. P. Sánchez-Marín, R. Villa and I. Giménez, *Biotechnol. Bioeng.*, 2018, **115**, 1604–1613.
21 S. Arndt, J. Seebach, K. Psathaki, H.-J. Galla and J. Wegener, *Biosens. Bioelectron.*, 2004, **19**, 583–594.
22 M.-H. Kim, D. Kim and J. H. Sung, *J. Ind. Eng. Chem.*, 2021, **101**, 126–134.
23 P. Shah, J. V. Fritz, E. Glaab, M. S. Desai, K. Greenhalgh, A. Frachet, M. Niegowska, M. Estes, C. Jäger, C. Seguin-Devaux, F. Zenhausern and P. Wilmes, *Nat. Commun.*, 2016, **7**, 11535.
24 S. J. Trietsch, E. Naumovska, D. Kurek, M. C. Setyawati, M. K. Vormann, K. J. Wilschut, H. L. Lanz, A. Nicolas, C. P. Ng, J. Joore, S. Kustermann, A. Roth, T. Hankemeier, A. Moisan and P. Vulto, *Nat. Commun.*, 2017, **8**, 262.
25 J. Yeste, X. Illa, C. Gutiérrez, M. Solé, A. Guimerà and R. Villa, *J. Phys. D: Appl. Phys.*, 2016, **49**, 375401.
26 L. Giampetruzzi, L. Blasi, A. Barca, E. Sciurti, T. Verri, F. Casino, P. Siciliano and L. Francioso, *Sens. Bio-Sens. Res.*, 2022, **37**, 100512.
27 J. Yeste, X. Illa, A. Guimerà and R. Villa, *A novel strategy to monitor microfluidic in-vitro blood-brain barrier models using impedance spectroscopy*, ed. S. van den Driesche, Barcelona, Spain, 2015, p. 95180N.

28 A. Guimerà, G. Gabriel, D. Parramon, E. Calderón and R. Villa, in *World Congress on Medical Physics and Biomedical Engineering, September 7-12, 2009, Munich, Germany*, ed. O. Dössel and W. C. Schlegel, Springer Berlin Heidelberg, Berlin, Heidelberg, 2009, vol. 25/7, pp. 868–871.
29 B. M. Maoz, A. Herland, O. Y. F. Henry, W. D. Leineweber, M. Yadid, J. Doyle, R. Mannix, V. J. Kujala, E. A. FitzGerald, K. K. Parker and D. E. Ingber, *Lab Chip*, 2017, **17**, 2294–2302.
30 N. Renous, M. D. Kiri, R. A. Barnea, R. Rauti, Y. Leichtmann-Bardoogo and B. M. Maoz, *Lab Chip*, 2022, **22**, 71–79.
31 R. Booth, *Lab Chip*, 2012, **12**, 1784.
32 C. Pitsalidis, A.-M. Pappa, A. J. Boys, Y. Fu, C.-M. Moysidou, D. van Niekerk, J. Saez, A. Savva, D. Iandolo and R. M. Owens, *Chem. Rev.*, 2022, **122**, 4700–4790.
33 C. Moysidou, C. Pitsalidis, M. Al-Sharabi, A. M. Withers, J. A. Zeitler and R. M. Owens, *Adv. Biol.*, 2021, **5**, 2000306.
34 D. A. Koutsouras, L. V. Lingstedt, K. Lieberth, J. Reinholz, V. Mailänder, P. W. M. Blom and P. Gkoupidenis, *Adv. Healthcare Mater.*, 2019, **8**, 1901215.
35 A. K. Waafi, N. Gaio, W. F. Quiros-Solano, P. Dijkstra, P. M. Sarro and R. Dekker, *IEEE Sens. J.*, 2020, **20**, 1150–1157.
36 A. Susloparova, S. Halliez, S. Begard, M. Colin, L. Buée, S. Pecqueur, F. Alibart, V. Thomy, S. Arscott, E. Pallecchi and Y. Coffinier, *Sens. Actuators, B*, 2021, **327**, 128895.
37 P. S. Nunes, P. D. Ohlsson, O. Ordeig and J. P. Kutter, *Microfluid. Nanofluid.*, 2010, **9**, 145–161.
38 L. C. Delon, Z. Guo, A. Oszmiana, C.-C. Chien, R. Gibson, C. Prestidge and B. Thierry, *Biomaterials*, 2019, **225**, 119521.
39 H.-Y. Tan, S. Trier, U. L. Rahbek, M. Dufva, J. P. Kutter and T. L. Andresen, *PLoS One*, 2018, **13**, e0197101.
40 X.-B. Wang, Y. Huang, P. R. C. Gascoyne, F. F. Becker, R. Hölzel and R. Pethig, *Biochim. Biophys. Acta, Biomembr.*, 1994, **1193**, 330–344.
41 K. S. Cole, *Membranes, ions, and impulses. A chapter of classical biophysics*, University of California Press, Berkeley, 1972.
42 M. D. Peterson and M. S. Mooseker, *J. Cell Sci.*, 1992, **102**, 581–600.
43 S. V. Nikulin, E. N. Knyazev, A. A. Poloznikov, S. A. Shilin, I. N. Gazizov, G. S. Zakharova and T. N. Gerasimenko, *Mol. Biol.*, 2018, **52**, 577–582.
44 A. Guimerà, E. Prats-Alfonso, R. Villa and F. J. del Campo, in *Electrochemical Strategies in Detection Science*, 2015, pp. 19–84.
45 M. Tomita, M. Hayashi and S. Awazu, *J. Pharm. Sci.*, 1996, **85**, 608–611.
46 C. B. Coyne, M. M. Kelly, R. C. Boucher and L. G. Johnson, *Am. J. Respir. Cell Mol. Biol.*, 2000, **23**, 602–609.